The Meteoritical Society

Meteoritics & Planetary Science 48, Nr 11, 2271–2288 (2013)
doi: 10.1111/maps.12187

Constraints on Vesta's elemental composition: Fast neutron measurements by Dawn's gamma ray and neutron detector

David J. LAWRENCE[1*], Patrick N. PEPLOWSKI[1], Thomas H. PRETTYMAN[2], William C. FELDMAN[2], David BAZELL[1], David W. MITTLEFEHLDT[3], Robert C. REEDY[2], and Naoyuki YAMASHITA[2]

[1]The Johns Hopkins University Applied Physics Laboratory, Laurel, Maryland, USA
[2]Planetary Science Institute, Tucson, Arizona, USA
[3]NASA Johnson Space Center, Houston, Texas, USA
[*]Corresponding author. E-mail: david.j.lawrence@jhuapl.edu

(Received 07 May 2013; revision accepted 11 July 2013)

Abstract–Surface composition information from Vesta is reported using fast neutron data collected by the gamma ray and neutron detector on the Dawn spacecraft. After correcting for variations due to hydrogen, fast neutrons show a compositional dynamic range and spatial variability that is consistent with variations in average atomic mass from howardite, eucrite, and diogenite (HED) meteorites. These data provide additional compositional evidence that Vesta is the parent body to HED meteorites. A subset of fast neutron data having lower statistical precision show spatial variations that are consistent with a 400 ppm variability in hydrogen concentrations across Vesta and supports the idea that Vesta's hydrogen is due to long-term delivery of carbonaceous chondrite material.

INTRODUCTION

One of the major objectives of NASA's Dawn at Vesta mission is to probe the relationship between Vesta and the howardite, eucrite, and diogenite (HED) meteorites (Russell and Raymond 2011; Russell et al. 2012). In addition, data from the Dawn mission are being used to investigate how Vesta's surface composition constrains the geological history of this planetary embryo. Data from all three instruments on Dawn—the visible and infrared (VIR) spectrometer, the framing camera (FC), and the gamma ray and neutron detector (GRaND)—have made significant progress toward these objectives. Results from the VIR and FC have shown spectral variations across Vesta's surface that are consistent with the presence of different HED-type materials (De Sanctis et al. 2012; Reddy et al. 2012). Specifically, these results indicate that the large Rheasilvia basin at Vesta's south pole is dominantly diogenitic in nature, whereas locations in more equatorward regions have a relatively larger eucrite component.

A variety of data sets from GRaND can be used to map elemental distributions across Vesta's surface. These measurements include elemental gamma ray lines, high-energy gamma rays (HEGRs), low-energy neutrons, epithermal neutrons, and fast neutrons. Iron, silicon, and oxygen elemental concentrations measured with gamma-ray data from GRaND are consistent with HED compositions and provide a conclusive elemental link between HED meteorites and Vesta (Prettyman et al. 2012; Yamashita et al. 2013). Analyses of iron concentrations, neutron absorption, and HEGRs support the presence of diogenitic materials in the Rheasilvia basin as well as enhancements of eucritic material in the central equatorial region of Vesta (Yamashita et al. 2013; Prettyman et al. 2013; Peplowski et al. 2013).

Initial results of fast neutron measurements at Vesta reported by Prettyman et al. (2012) indicated that fast neutron variations were dominated by hydrogen variations across Vesta's surface, but with an inferred hydrogen concentration approximately a factor of two larger than that derived using epithermal neutrons. In this study, we carry out a full analysis of GRaND fast neutron data from the Low Altitude Mapping Orbit (LAMO) portion of Dawn's Vesta mission. We first provide a background discussion of the compositional

information revealed by fast neutrons. Next, we describe how GRaND measures fast neutrons. We then give details of the GRaND fast neutron data reduction and analysis. Finally, we provide a discussion and summary.

PLANETARY FAST NEUTRONS

Planetary fast neutrons that can be used to infer the composition of planetary surfaces are created by nuclear spallation reactions of galactic cosmic rays (GCR) with regolith materials within about a meter of the surfaces of airless or nearly airless planetary bodies. In practice, fast neutrons are defined approximately as having energies (E_n) greater than 0.5 MeV, which contrasts with lower energy epithermal (0.4 eV < E_n < 0.5 MeV) and thermal (E_n < 0.4 eV) neutrons (e.g., Prettyman et al. 2011; Lawrence et al. 2013). Planetary fast neutrons were first measured at the Moon using a scintillator sensor that was part of the Lunar Prospector gamma-ray spectrometer (LP-GRS) (Feldman et al. 1998; Maurice et al. 2000). In addition to the Moon, fast neutrons have also been measured at Mars (e.g., Maurice et al. 2011) and Mercury (Lawrence et al. 2013).

The initial fast neutron measurements at the Moon showed relatively large count rate variations that spatially correlated with lunar iron and titanium concentrations (Maurice et al. 2000). Gasnault et al. (2000) carried out particle transport simulations to establish that fast neutrons should dominantly vary with iron and titanium concentrations. Gasnault et al. (2001) extended this analysis to demonstrate that fast neutrons provide a robust measure of the average atomic mass (<A>) of a planetary regolith. <A> is defined using:

$$\frac{1}{<A>} = \sum_{i=1}^{n} \frac{w_i}{A_i} \quad (1)$$

where w_i and A_i are the weight fraction and atomic mass of the ith of n elements. This correlation of fast neutrons with <A> is valid only for planetary materials that contain little to no hydrogen (Gasnault et al. 2000, 2001), as is generally the case for nonpolar lunar regolith. For Mars, which contains larger amounts of hydrogen at all locations (Feldman et al. 2002) in comparison to the Moon (e.g., Lawrence et al. 2006), variable hydrogen concentrations are the dominant source of variations in fast neutrons (e.g., Maurice et al. 2011). For planetary surfaces that contain soils with enhanced hydrogen buried under tens of centimeters thick layers of lower hydrogen soils, combined measurements of epithermal and fast neutrons can constrain the burial depth of the hydrogen-rich layer (e.g., Prettyman et al. 2004; Feldman et al. 2007; Lawrence et al. 2013).

Vesta presents an interesting scenario for planetary fast neutrons. As shown with measurements of epithermal neutrons, Vesta has variable hydrogen concentrations across its surface of at least 400 ppm H (Prettyman et al. 2012). While not nearly as large as the concentrations at Mars (i.e., greater than 2 wt% water equivalent hydrogen [WEH] or 2222 ppm H) (Maurice et al. 2011), the spatial footprint-averaged hydrogen variations at Vesta are about a factor of four larger than similar footprint average values of 100–150 ppm H seen at the Moon's polar regions (Lawrence et al. 2006). Such variations should be detectable using fast neutrons with at least a 4% count rate variation based on the fast neutron-to-WEH variation derived by Feldman et al. (1998). Initial zonal variations in fast neutrons due to hydrogen were reported (Prettyman et al. 2012). At the same time, nonhydrogen elemental variations across Vesta are expected to result in corresponding variations in <A>. Prettyman et al. (2011) provided an initial documentation of <A> variations within HED meteorites and found a variation in <A> from approximately 21.7 to 23 atomic mass units (amu), with lower values corresponding to diogenites and higher values corresponding to basaltic eucrites. Gasnault et al. (2001) showed that count rates from fast neutrons vary roughly by 10% per amu for lunar materials. Thus, depending on Vesta's compositional heterogeneity and GRaND's spatial smoothing (Prettyman et al. 2011), the fast neutron flux at Vesta could vary by up to approximately 10% due to nonhydrogen elemental variations.

FAST NEUTRONS AS MEASURED BY GRAND

GRaND measures both gamma rays and neutrons in a single instrument using a combination of plastic and inorganic scintillators as well as solid-state sensors (Prettyman et al. 2011). GRaND measures fast neutrons using borated plastic scintillators of the same type that have measured fast neutrons at the Moon (Feldman et al. 2004), Mars (Boynton et al. 2004), and Mercury (Goldsten et al. 2007). Fast neutrons are detected and identified using a coincidence double pulse technique (see fig. 16 of Prettyman et al. 2011). An initial prompt pulse caused by energy loss of recoil protons from neutron moderation in the scintillator provides a measure of the incident neutron energy. A delayed neutron capture pulse unambiguously identifies a neutron event via its energy from the $^{10}B(n,\alpha)$ reaction along with its 2 μs characteristic time delay from the

prompt pulse. Thus, characteristic signatures of a fast neutron detection include a 2 μs exponential decay of the event time-to-second pulse (TTSP) as well as a 93 keV electron-equivalent energy peak from the $^{10}B(n,\alpha)$ reaction (Prettyman et al. 2011).

GRaND contains four separate scintillator sensors that measure fast neutrons. In addition to measuring fast neutrons, these same scintillators serve as anticoincidence shields for GRaND's central gamma-ray sensors. Two of the scintillators labeled +Z and −Z (to designate the direction they point in the spacecraft fixed coordinate system) are oriented in the nadir (+Z) and antinadir (−Z) directions during nominal science data acquisition in LAMO. These borated plastic scintillators are optically coupled to Li-loaded glass scintillators to make a phosphor sandwich ("phoswich") that measures thermal and epithermal neutrons. Because of its orientation, the +Z sensor provides the primary measure of Vesta fast neutrons. The −Z sensor is oriented to provide a measure of spacecraft-generated neutrons. The other two borated plastic scintillators are labeled +Y and –Y, as they face in the spacecraft plus and minus Y directions, respectively. These scintillators are not coupled to other scintillators. The +Y sensor looks away from the Dawn spacecraft in the direction of the +Y solar panel and therefore has some sensitivity to Vesta neutrons. However, because it does not directly face Vesta during nominal operations, its sensitivity to Vesta neutrons is significantly less than the +Z sensor. The −Y sensor obliquely views the top deck of the Dawn spacecraft and, as a consequence, does not have a large sensitivity to Vesta neutrons. We note that the Z and Y sensors have separate electronic signal chains for sensor read out (Prettyman et al. 2011).

Gasnault et al. (2001) show that fast neutron variations from a dry planetary body (e.g., the Moon) are best correlated with variations in <A>. We have tested this behavior for expected fast neutron variations in HED meteorites. Using the particle transport code MCNPX (Pelowitz 2007), energy-dependent neutron fluxes were calculated for 57 HED elemental compositions compiled by Usui and McSween (2007) and Usui et al. (2010). To obtain relative fast neutron count rates, the calculated neutron fluxes were convolved with a borated plastic fast neutron efficiency response in a manner similar to that carried out by Lawrence et al. (2013). Figure 1 shows the resulting relative fast neutron count rate versus <A> for each meteorite composition. We note that the original compositions did not always sum to a weight fraction of 1, but varied from 0.98 to 1.025. MCNPX uses normalized input compositions, where each element's concentration is weighted by the summed weight fraction for each of the 57 compositions. As a consequence, the <A> values used in Fig. 1 have been adjusted for the normalized concentrations. Figure 1 shows a reasonable correlation between the two sets of values (overall correlation coefficient of 0.88), which generally confirms the fast-neutron-to-<A> relationship identified by Gasnault et al. (2001). However, within some meteorite types (e.g., cumulate eucrite, polymict eucrite, and howardite), the correlation between <A> and fast neutron count rate is less clear. This lack of correlation is not likely due to statistical uncertainties within the particle transport simulations, as there is a tight correlation for the basaltic eucrites, which used the same number of particle transport histories as was used for the other meteorite groups.

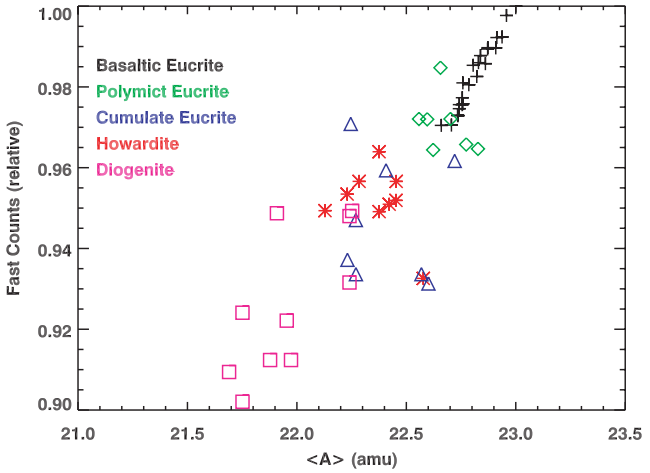

Fig. 1. Average atomic mass, <A>, versus calculated fast neutron count rates for a borated plastic scintillator. Different colors and symbols represent different types of HED meteorites. Elemental concentrations are taken from Usui and McSween (2007) and Usui et al. (2010).

Finally, as mentioned by Gasnault et al. (2001), the <A> versus fast neutron correlation does not necessarily hold when soils contain enhanced hydrogen concentrations. However, Gasnault et al. (2001) did not investigate <A> variations for the moderate hydrogen concentrations seen at Vesta. To investigate this issue, neutron fluxes were calculated for mean HED compositions with varying amounts of WEH. Figure 2 shows derived fast neutron count rates versus WEH concentrations relevant to Vesta. The vertical gray line at 0.0036 weight fraction WEH illustrates the fast neutron variation due to the 400 ppm H variation on Vesta if the low hydrogen value is zero ppm H. For constant <A>, the variation due to hydrogen is 5%, which is slightly larger than the 4% derived using the fast neutron-to-WEH relation of Feldman et al. (1998). If the baseline hydrogen concentration is 400 ppm H instead of zero, an additional 400 ppm H variation across Vesta would still cause a 4.5% variation in fast

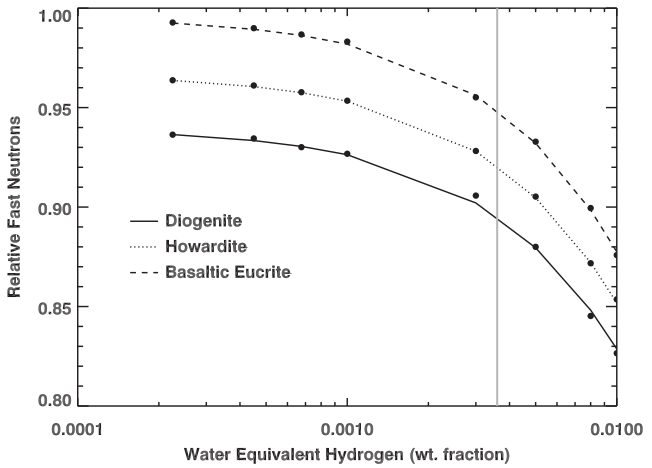

Fig. 2. Calculated relative fast neutron count rates versus water-equivalent hydrogen concentration for the three primary HED meteorite types of diogenite (solid line), howardite (dotted line), and basaltic eucrite (dashed line). The fast neutron count rates are relative to the maximum nonhydrogen case for basaltic eucrites. The vertical gray line shows the maximum hydrogen concentration at Vesta if the low hydrogen value is zero ppm hydrogen.

neutrons. In contrast, the fast neutron variation from average diogenite to basaltic eucrite compositions is around 6%. Thus, the magnitude of fast neutron variation due to hydrogen is slightly smaller than that expected from <A>. Furthermore, Fig. 2 shows that the relative fast neutron variations from hydrogen do not depend on <A>. As a consequence, variations from hydrogen and <A> can be treated in a separable manner such that if hydrogen variations can be independently known (e.g., using epithermal neutrons), then <A> variations can be determined.

FAST NEUTRON MEASUREMENTS

Calibration and Vesta Fast Neutron Pulse Signatures

Prettyman et al. (2011) reported GRaND fast neutron calibration data taken prior to the Dawn launch. With these data, Prettyman et al. (2011) showed that the behavior of the TTSP histogram deviated from the standard 2 μs decay time for early TTSP values. Specifically, for TTSP values less than 3–4 μs, the GRaND fast neutron sensors exhibit peaks that rise above the 2 μs exponential decay. According to Prettyman et al. (2011), this count rate enhancement at low TTSP values is due to a process called afterpulsing, where the photomultiplier tube (PMT) that observes the scintillator emits a low-amplitude "afterpulse" that is caused by ionization of residual gas in the PMT. Typically, afterpulsing effects can be eliminated by removing second pulses that have low amplitudes. Prettyman et al. (2011) demonstrated the validity of this afterpulse removal process for the −Y sensors; however, this removal process did not remove the apparent afterpulsing in the +Z sensor. Prettyman et al. (2011) stated that if this apparent afterpulsing behavior of the +Z sensor is not adequately understood, then a possible way to remove these counts is to only use data with TTSP values greater than 4 μs. While such a solution would cleanly remove afterpulsing counts, it has the drawback that it would also remove over 70% of the measured counts, which would significantly reduce the statistical precision of the measured data.

We have revisited the afterpulsing analysis of Prettyman et al. (2011) using Vesta LAMO data. The details of the analysis are given in the Appendix, but a summary is described here. TTSP and second pulse spectra from the +Z sensor are shown in Fig. 3 and similar spectra for the −Y sensor are shown in Fig. 4. Here, the same type of afterpulsing removal process has been applied to both sensors, and the behavior of the sensors is the same as was observed with the calibration data. The −Y sensor shows a reasonably good 2 μs decay time behavior for all but the lowest TTSP values, while there is a significant peak at low TTSP values for the +Z sensor. The second pulse spectra for both sensors shows a clear peak that is due to the $^{10}B(n,\alpha)$ reaction and a sharp cutoff at low channels showing where the afterpulse removal was applied. We note that the TTSP behavior of the +Y sensor is identical to that of the −Y sensor; the TTSP behavior of the −Z sensor is identical to that of the +Z sensor.

As discussed in the Appendix, we conclude that afterpulsing best describes the full behavior of the Y sensors. However, for the Z sensors, we conclude there is an additional effect that is contributing to the peak at low TTSP values. Given that this effect presents itself in an identical manner for both Z sensors, but not for the Y sensors, we conclude that this effect is not due to afterpulsing and is probably due to effects from a combination of the Li glass borated plastic phoswich arrangement and/or the electronics used to read out the Z sensors (Prettyman et al. 2011). At this time, we do not know the exact cause of this TTSP effect, but will proceed in the analysis using two parallel paths. For the first path, we define a baseline +Z sensor data set where we apply the same afterpulsing removal algorithm as that which successfully works for the Y sensors. This baseline +Z data set has good statistical precision, but an uncertain behavior for low TTSP values. For the second path, we define a restricted +Z data set where we limit TTSP values to be greater than 4 μs. This restricted data set has a significantly poorer statistical precision than the baseline data set. Aside from the

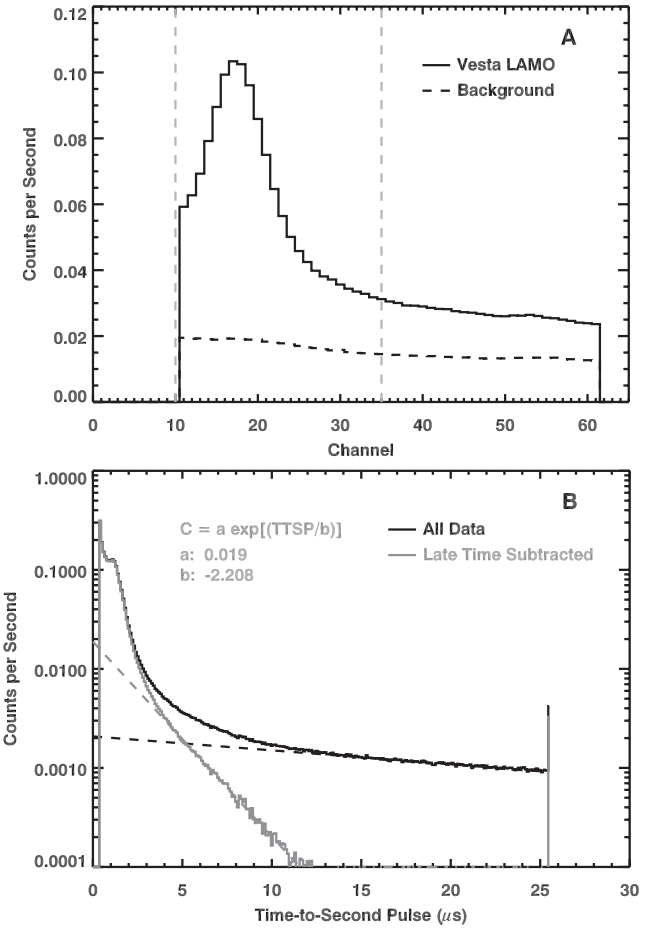

Fig. 3. A) Histogram of second pulse pulse-height data from the +Z borated plastic scintillator. Solid line shows data from Vesta LAMO; dashed line shows background data when the Dawn spacecraft was not near Vesta. The peak near channel 18 identifies the $^{10}B(n,\alpha)$ reaction in the borated plastic scintillator. Vertical dashed lines show the channel limits that define the measured fast neutron count rates. B) Histogram of average TTSP values for Vesta LAMO from the +Z sensor. Solid line shows all data; gray line shows data after the late-time background has been subtracted. Dashed lines show exponential fits to both the late-time background and background-subtracted TTSP values. The late-time subtracted values show a 2.2 μs exponential decay time fit for TTSP values greater than 4 μs. The late-time subtracted TTSP data deviate from the 2.2 μs decay time for TTSP values less than 4 μs.

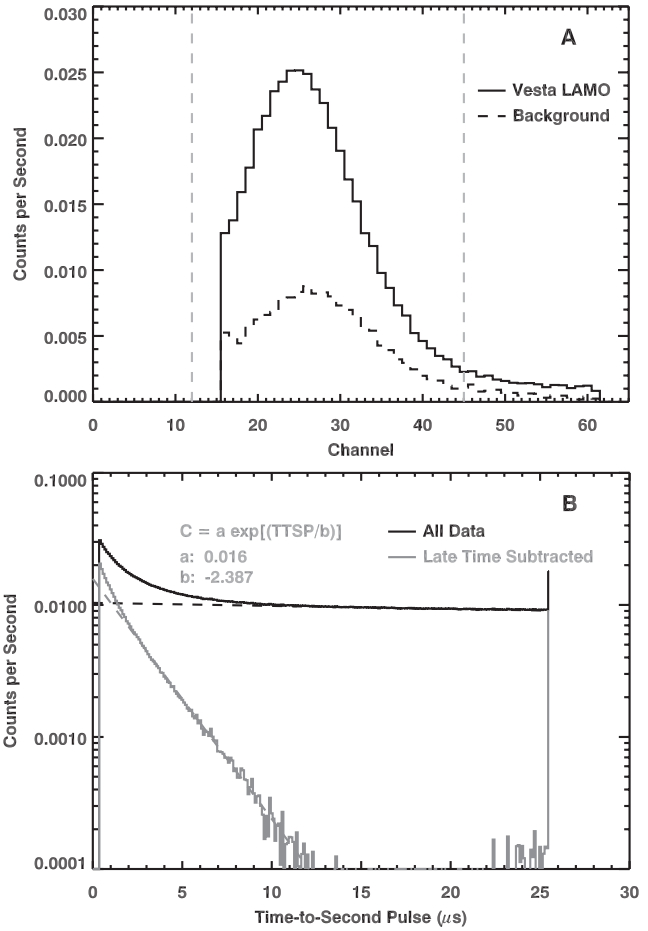

Fig. 4. Same data as for Fig. 3 but for the −Y borated plastic scintillator.

different TTSP restrictions and final spatial binning, the two data sets are analyzed in an identical manner.

Finally, we note the possibility that the Y sensors could, in principle, be used as independent measures of fast neutrons. To investigate this possibility, we analyzed data from both the plus and minus Y sensors and found that the combination of low Vesta counts and high spacecraft background resulted in count rate maps that were greatly limited in statistical precision. Data from the Y sensors are therefore not being used further in this analysis.

Fast Neutron Data Reduction

The data reduction process for the GRaND fast neutrons is similar to that used for other reported GRaND data sets (Prettyman et al. 2012, 2013; Peplowski et al. 2013; Yamashita et al. 2013). Items specific to the fast neutron data reduction are described here. The fast neutron reduction starts with a series of data selections to obtain a data set suitable for additional analysis. As described in the prior GRaND papers, the GRaND data set is divided into a number of time epochs, where each epoch is delineated by characteristics, such as the absence or presence of solar energetic particles, and various instrument settings, such as the +Z PMT high voltage. Based on a preanalysis of the fast neutron data, and taking into account the factors mentioned above, we arrived at the final selection of two time-contiguous data sets for the fast

neutron analysis. Time period 1 ranges from 9 December 2011 00:00:00 to 14 January 2012 06:48:00; time period 2 ranges from 3 April 2012 00:00:00 to 1 May 2012 01:51:29. In addition to the time selection, a nadir angle selection was applied where only nadir angles less than 3º were allowed (nadir angle is defined here as the angle between the spacecraft +Z axis and the spacecraft nadir look direction). After these selections, the complete data set contains 64,732 separate measurements, where each measurement is a 70 s accumulation interval.

After the data selections, a number of data corrections are applied to the data. We have empirically found that the period 1 and period 2 data differ by a scale factor such that the time series corrections described just below need to be applied separately to each data set. The +Z PMT high voltage had different values for periods 1 and 2, which is the probable reason why this scale factor is needed to normalize the two data sets. The primary data set consists of the summed counts between channels 10 and 35 in the second pulse spectra (Fig. 3a). The total counts, C_T, contain Vesta neutrons, C_V, and background neutrons, C_B, generated from GCRs hitting the Dawn spacecraft material. These counts vary with altitude according to:

$$\begin{aligned} C_T(h) &= C_V(h) + C_B(h) \\ &= C_{Vo}\Omega(h) + C_{Bo}[1 - \Omega(h)]\,. \end{aligned} \quad (2)$$

Here, $\Omega(h)$ is the solid angle subtended by Vesta as viewed by GRaND. A derivation of $\Omega(h)$ that takes into account Vesta's nonspherical shape is given by Prettyman et al. (2011, 2012) and used here. Equation 2 assumes that C_{Bo} is constant so that the total background contribution to C_T goes down as Vesta blocks portions of the GCR flux that hit the spacecraft. C_{Bo} is empirically determined using an iterative process, where the total counts are plotted versus solid angle. A linear regression is applied to the data and the C_{Bo} is assigned the offset value in the regression. The Vesta counts, $C_V(h)$, are then obtained by subtracting the solid angle-weighted background counts from the total counts.

Next, the background-subtracted counts are corrected for solid angle variations. To characterize the quantitative solid angle dependence, only data poleward of 60ºN are used to avoid biases from the topographically and compositionally distinct Rheasilvia basin (De Sanctis et al. 2012; Prettyman et al. 2012; Reddy et al. 2012). Figure 5a shows these latitude-selected data plotted versus solid angle, along with solid-angle binned data. These data follow a linear trend of $C_V = C_{Vo}\Omega$, where C_{Vo} is an empirically determined constant. The data are corrected using $C_{V,\Omega} = C_V - C_{Vo}\Omega + C_{Vo}\Omega_o$ where $\Omega_o = 1$. The added offset corrects the data to the equivalent count rate at $\Omega = 1$ sr. Figure 5b shows the uncorrected and solid angle-corrected data, where the data have been smoothed in solid angle to reduce statistical variations and better illustrate the solid angle variations.

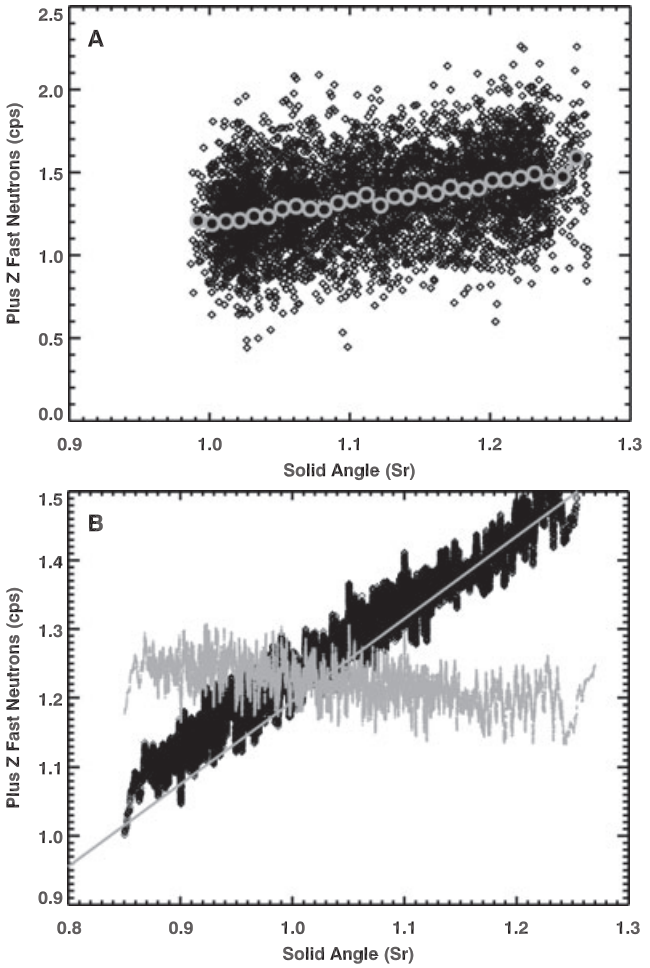

Fig. 5. A) +Z baseline fast neutron count rates selected for Vesta latitudes greater than 60ºN versus the solid angle subtended by Vesta in the GRaND instrument (black diamonds). Open gray circles show solid-angle binned values of the same count rates. B) Black diamonds show all accepted +Z baseline fast neutron data smoothed in solid angle and plotted versus solid angle prior to correction for solid angle. Solid gray line shows the fit derived using the 60ºN data. Gray diamonds show solid angle-corrected data, again smoothed in solid angle.

The next correction is for variations in the GCR flux. As with prior studies, we use the GRaND triple coincidence counter as the GCR proxy, P_{GCR}. Figure 6 shows the variation of solid angle-corrected counts versus the GCR proxy. After fitting the GCR proxy versus fast neutron count rate with a linear regression, the fast neutrons were corrected for GCR variations

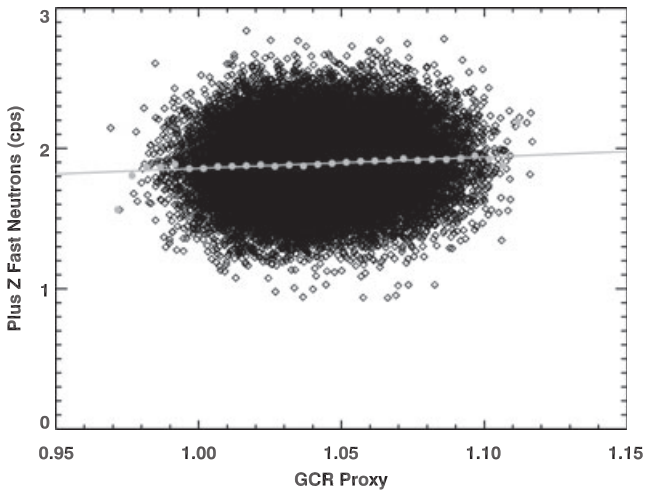

Fig. 6. Solid angle-corrected +Z baseline fast neutron data plotted versus the GCR proxy, which is the relative variation of GRaND triple coincidence counts. Gray circles show GCR-proxy binned values of the count rates. Solid gray line shows a linear fit to the binned values.

using, $C_{V,\Omega,GCR}/(aP_{GCR} + b)$, where a and b are the fitted constants to the GCR proxy. As a final correction, a scale factor of 0.8 was applied to the data in period 2 to account for the scale factor difference mentioned previously.

RESULTS

Analysis of Baseline +Z Sensor Data Set

With the time series corrections complete, the corrected fast neutrons can be mapped across the surface of Vesta. In this subsection, we discuss the baseline +Z sensor data set; in the next subsection, we discuss the TTSP-restricted +Z sensor data set. Figure 7 shows the corrected fast neutrons binned in approximately equal area pixels that have a size of 20º by 20º at the equator. The data were originally binned in 5º by 5º equal area pixels, spatially smoothed using a two-dimensional Gaussian function with a sigma width of 600 km, then rebinned to the 20º sized pixels. There are clear count rate variations, with maximum count rates seen in Rheasilvia basin and minimum count rates seen in the equatorial region centered on longitude 180ºE and the north polar region. This map of fast neutrons can be compared with a map of epithermal neutrons (Prettyman et al. 2012), which is reproduced in Fig. 8 using the same pixel sizes as used in Fig. 7. While there are differences between the maps, there is a clear correspondence between the two measurements, with both showing high count rates in Rheasilvia basin and low counting rates in the central equatorial region. The correspondence between the two data sets is made more explicit as a scatter plot, where a strong correlation between the measured epithermal and +Z baseline fast neutrons is observed (Fig. 9).

Because the variations in epithermal neutrons have been attributed to surface variations in hydrogen (Prettyman et al. 2012), it is natural to expect that some portions of the measured variations in +Z baseline fast neutrons are also due to hydrogen variations. We can test this hypothesis by using the +Z baseline fast neutron measurements to derive an independent estimate of hydrogen concentrations. Such an estimate can be made using a fast neutron dynamic range as constrained by the observed correlation between the +Z baseline fast neutrons and the epithermal neutron measurements. This fast neutron count rate dynamic range (minimum and maximum values) is then used in equation 1 of Prettyman et al. (2012) along with a calibration constant, k, to derive a lower limit hydrogen concentration. Prettyman et al. (2012) used separate calibration constants for epithermal and fast neutrons.

To determine the dynamic range of +Z baseline counts that is due to variations in hydrogen, expected variations in both hydrogen and <A> need to be considered because both hydrogen and <A> may result in a fast neutron variation of similar size (Fig. 2). In particular, we note that the location on Vesta with the largest hydrogen concentrations has also been observed to have the largest fraction of basaltic eucritic material (e.g., De Sanctis et al. 2012; Reddy et al. 2012; Peplowski et al. 2013; Prettyman et al. 2013; Yamashita et al. 2013). As shown in Fig. 1, basaltic eucrite material is also expected to have the largest <A> values, and, by implication, the highest nonhydrogen-related fast neutron counts. Therefore, although fast neutron variations from <A> and hydrogen are formally separable (Fig. 2), the specific distribution of both <A> and hydrogen on Vesta might still introduce biases into the measured data.

The gray data points in Fig. 9 show the count rates from the high-hydrogen region delineated by a latitude boundary of 45ºS to 60ºN and longitude boundary of 35ºE to 115ºE. Although these data points have both low +Z baseline fast neutrons and epithermal neutrons, they still lie above a trend line defined by the remaining data outside the high-hydrogen region. This observation suggests that the data from the high-hydrogen region should not be used to define the epithermal to +Z baseline fast neutron trend from which a fast neutron dynamic range is derived, as nonhydrogen elemental variations within the high-hydrogen region only affect the fast neutron counting rates and not epithermal neutron counting rates. Rather, we use the linear trend

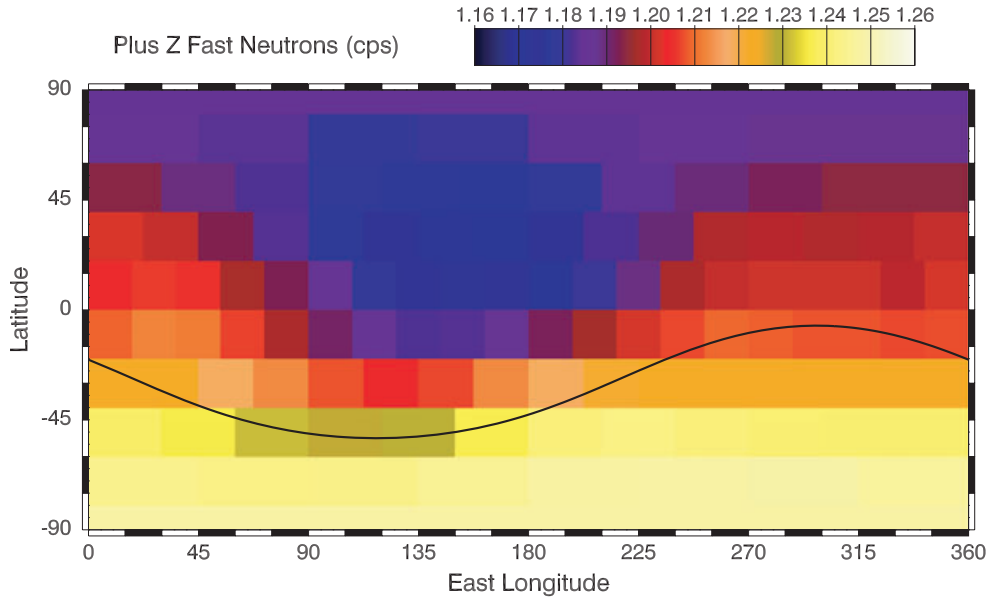

Fig. 7. Cylindrical projection map of +Z baseline fast neutrons in counts per second on Vesta's surface using the Claudia coordinate system (Russell et al. 2012). Solid line shows the approximate boundary location of Rheasilvia basin. Pixels are approximately equal area and have a size of 20º by 20º at the equator.

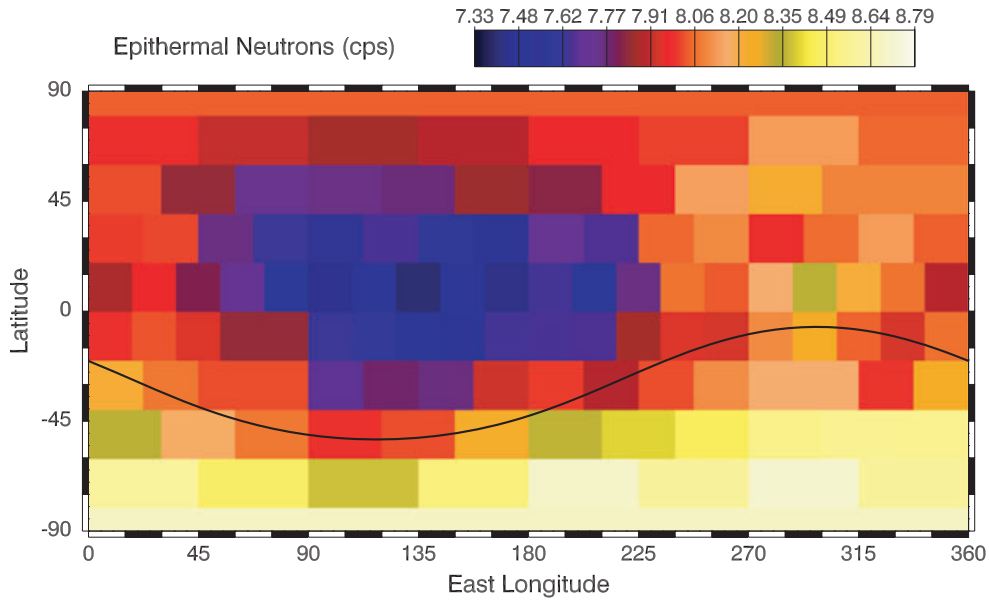

Fig 8. Cylindrical projection map of GRaND epithermal neutrons (Prettyman et al. 2012) rebinned to the same pixel sizes as Fig. 7.

line shown in Fig. 9. Given the fact that fast and epithermal neutrons will vary with hydrogen using the same functional form but different calibration constants for a relatively limited range of hydrogen concentrations (Feldman et al. 1998; Prettyman et al. 2012), a linear trend line is appropriate. For minimum and maximum epithermal neutron count rates of 7.4 and 8.7 cps, respectively, the trend line implies a +Z baseline fast neutron maximum-to-minimum fraction of 1.10. When this value is used for C_o/C in equation 1 of Prettyman et al. (2012), and k = 11200 is used as the fast neutron calibration constant of the same equation, the derived hydrogen concentration is 1200 ppm H. This is significantly larger than the value of 400 ppm H derived using epithermal neutrons. Based on the physics of neutron transport, it is difficult to conceive a scenario

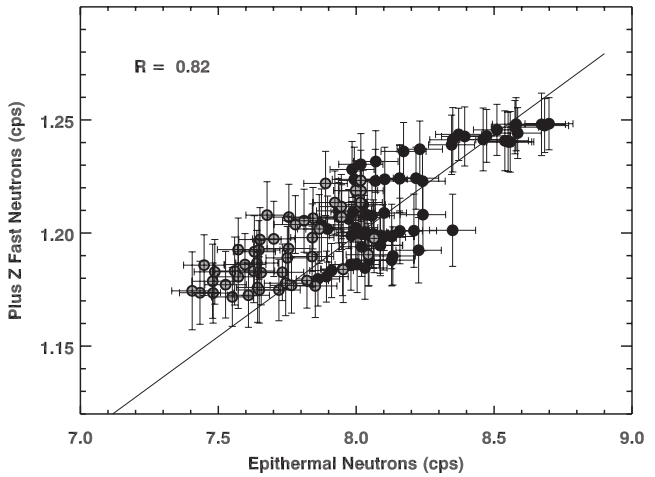

Fig. 9. Scatter plot of epithermal neutrons versus +Z baseline fast neutrons. Gray data points show data taken from a boundary region (45ºS to 60ºN and 35ºE to 115ºE) that covers the low epithermal neutron count rate and high-hydrogen region identified by Prettyman et al. (2012). Black data points show data taken from the remaining locations. Error bars show statistical uncertainties. Solid black line shows trend line as defined by the black data points.

where fast neutron variations would indicate larger inferred hydrogen content than epithermal neutrons.

A possible explanation for this discrepancy is that there might be a signal contamination of epithermal neutrons in the +Z baseline fast neutron data set. While a mechanism for the inclusion of such a component is not fully understood, multiple lines of evidence point to such a conclusion. First, the counts that are being measured have a clear signature from a neutron capture $^{10}B(n,\alpha)$ reaction as shown in Fig. 3a. Such neutron capture reactions are created from both fast and epithermal neutrons. Second, the +Z baseline neutrons have an unexplained TTSP behavior at low TTSP values that deviates from standard fast neutron detections. This TTSP behavior also does not have the expected characteristics of afterpulsing as is described in the Appendix. Third, as is shown in the next section, a lower limit hydrogen concentration of 405 ± 220 can be derived using the TTSP-restricted fast neutrons. While this estimate has large uncertainties, it is lower than the minimum hydrogen concentration derived using the +Z baseline fast neutrons and is consistent with the values derived using epithermal neutrons. Finally, if we assume that the +Z baseline fast neutrons do contain an epithermal neutron component, Equation 1 of Prettyman et al. (2012) can be inverted using [H] = 400 ppm to derive an empirical calibration constant. When this is done, we find k = 4100, which is much closer to the calibration constant used for epithermal neutrons in Prettyman et al. (2012) (k = 2100) than for fast neutrons.

The existence of a substantial epithermal neutron component within the +Z baseline fast neutron data set does not preclude the possibility of deriving nonhydrogen composition variations from this data set. As Fig. 9 shows, the equatorial region with a large fraction of basaltic eucrite material also shows a relatively higher count rate than the trend would imply from regions with less basaltic eucrite material. To formally investigate the nonhydrogen variations, we have detrended the +Z baseline fast neutrons, $C_{+Z,\mathrm{baseline}}$, to obtain a residual map, C_{resid}, using

$$C_{\mathrm{resid}} = C_{+Z,\mathrm{baseline}} - \left(dC_{\mathrm{epi}} + e\right) + \left(d\left[C_{\mathrm{epi}} = 8\mathrm{cps}\right] + e\right). \quad (3)$$

Here, d and e are the linear fit parameters for the trend line of Fig. 9 and we add an arbitrary offset at C_{epi} = 8 cps. The detrended map is shown in Fig. 10.

When the detrended map is compared with other measures of nonhydrogen compositional variations, we find a reasonably good correspondence. Specifically, the highest residual counts are found in the central equatorial region, a region that has also been shown to have enhanced HEGRs (Peplowski et al. 2013), neutron absorption (Σ_{eff}) (Prettyman et al. 2013), and Fe abundances (Yamashita et al. 2013). All these measures are consistent with the presence of a large fraction of basaltic eucrite material. Figure 10 shows relatively low counts within the Rheasilvia basin, which is consistent with the presence of a larger fraction of diogenite material within the basin compared with other locations. Again, this is consistent with other measures of compositional variations. Finally, Fig. 10 shows relatively low residual counts in the north polar region and in a lane that extends from the north along longitude 315ºE.

Figure 11 shows a histogram of the residual counts. The maximum-to-minimum dynamic range of these counts is 1.23/1.17 = 1.05, or 5%. This measured variation is consistent with a footprint-averaged variation of <A> for HED meteorites (Fig. 1).

Analysis of +Z TTSP-Restricted Data Set

To investigate the possibility that the +Z sensor baseline data set might contain a substantial epithermal neutron component, we have analyzed a TTSP-restricted data set. Specifically, we have imposed a TTSP selection on the +Z data set such that only events with TTSP values greater than 4 μs are considered. This retains events having a standard fast neutron 2 μs TTSP decay, but greatly reduces the statistical precision. The analysis of this data set was carried out using the

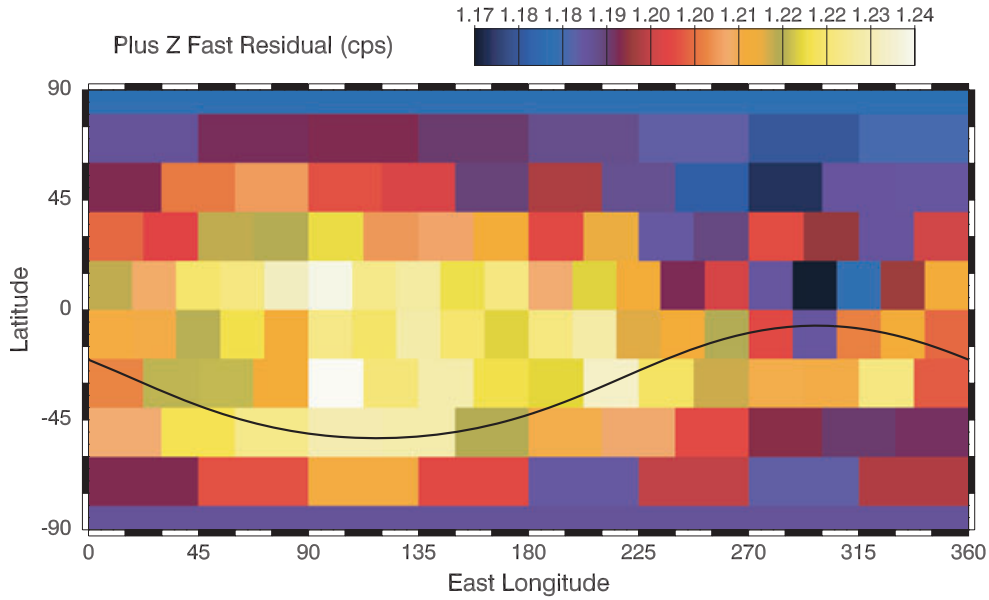

Fig. 10. Cylindrical projection map of +Z baseline residual fast neutrons, C_{resid}, using same pixel sizes as for Fig. 7.

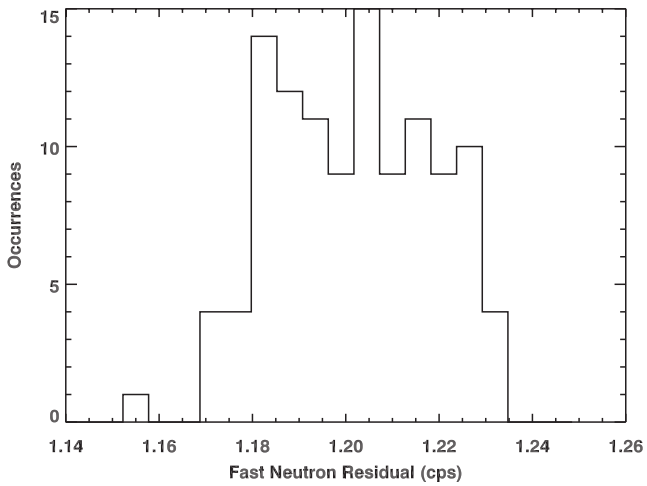

Fig. 11. Histogram of C_{resid} values.

identical steps as were used in the +Z sensor baseline data set. However, because the statistical precision is poorer, the TTSP-restricted data have been mapped on 40° by 40° pixels instead of 20° by 20° pixels.

Figures 12, 13, and 14 show the TTSP-restricted count rate map, the scatter plot of this map versus epithermal neutrons, and a residual map that results from the detrending of epithermal neutrons from the data of Fig. 12. Due to the significantly lower count rates, there is much less spatial contrast in this map than the +Z baseline map. The correlation with epithermal neutrons is less pronounced, having a correlation coefficient of 0.35 compared to 0.81 for the +Z baseline data set. Nevertheless, a linear regression line does show a positive slope (gray line in Fig. 13). When this line, along with the one-sigma uncertainties on the fit parameters, and the fast neutron calibration constant are used to derive a hydrogen concentration, we find [H] = 405 ± 220 ppm. This is over a factor of two lower than the values derived using the +Z baseline data set. While the uncertainty of this derived hydrogen concentration is large, it is statistically consistent with the hydrogen concentration derived using epithermal neutrons. This result provides evidence that the epithermal neutron component that appears to be present in the +Z baseline data set is significantly reduced or absent from the TTSP-restricted data set. Finally, while the scatter is large in the TTSP-restricted residual map (Fig. 14), it does show enhancements and reductions are qualitatively consistent with that of the higher fidelity +Z baseline residual map. This map therefore provides evidence that both residual maps are measuring nonhydrogen compositional variations related to <A>.

DISCUSSION

We have presented a full analysis of GRaND fast neutron data from the Dawn LAMO mission. From this analysis, we have obtained compositional information about Vesta that we discuss and summarize here.

Variation of Measured Fast Neutrons with Epithermal Neutrons

There is strong evidence that the +Z baseline fast neutron data set contains a substantial component of

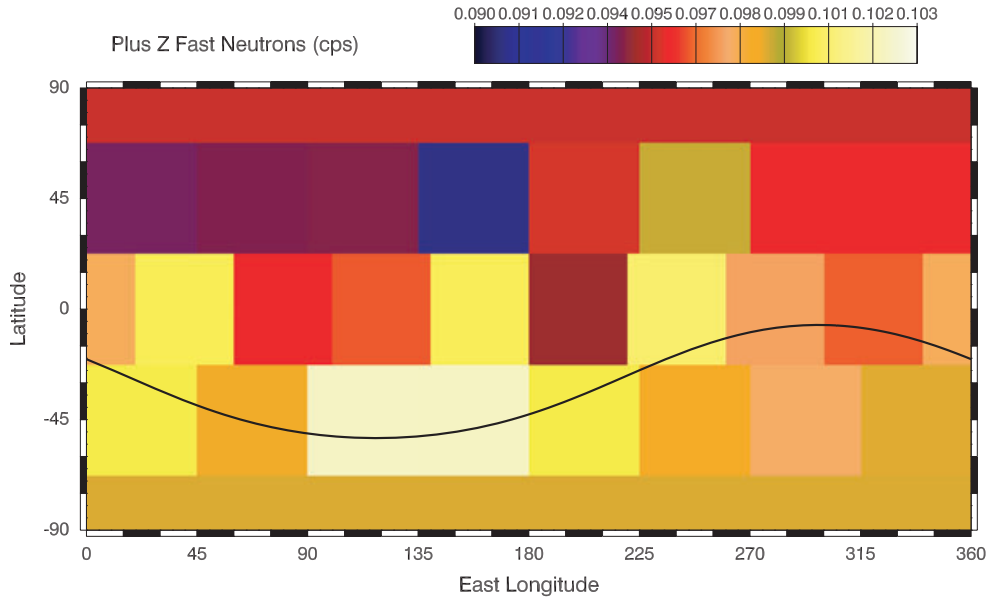

Fig. 12. Cylindrical projection map of +Z TTSP-restricted fast neutrons using approximately equal area pixels that have a size of 40° by 40° at the equator.

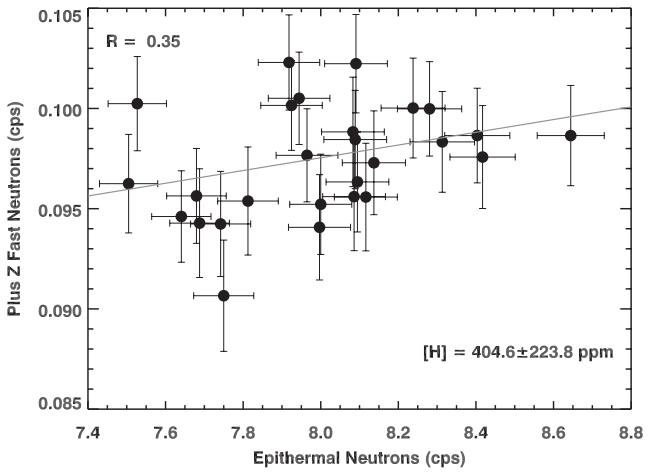

Fig. 13. Scatter plot of +Z TTSP-restricted fast neutrons from Fig. 12 versus epithermal neutrons binned into the same pixels. Solid line shows linear regression for the data points. The correlation coefficient for the data points of 0.35 is shown.

epithermal neutrons. The exact measurement/instrumentation mechanism for this component is not clearly understood. The TTSP-restricted data set, albeit with poorer statistical precision, does not show evidence for a strong epithermal neutron component. Rather, the TTSP-restricted data set shows a modest correlation with epithermal neutrons, which could result from hydrogen variations on Vesta's surface. The hydrogen concentration derived from the signal dynamic range is consistent, within one-sigma statistical uncertainties, with the hydrogen concentration derived from epithermal neutrons (Prettyman et al. 2012). This agreement between the hydrogen concentrations derived from epithermal neutrons and the TTSP-restricted fast neutrons supports the idea that the hydrogen on Vesta is not layered, but is uniformly distributed within the top tens of centimeters of material. Such a uniform distribution is consistent with the hypothesis suggested by Prettyman et al. (2011, 2012) that hydrogen on Vesta is due mostly to the long-term accumulation of carbonaceous chondrites.

Variation of Residual Fast Neutrons with HED and Vesta Elemental Concentrations

Regardless of the source of the +Z baseline fast neutron-versus-epithermal neutron correlation, this correlation can be detrended and the resulting residual map (Fig. 10) shows clear compositional variability. We can investigate what this variability reveals about primary elemental variations across Vesta as well as compare this map with other orbital measures of Vesta surface composition. Figure 15 shows variations of <A> versus four different composition measures for the 57 HED meteorite compositions of Usui and McSween (2007) and Usui et al. (2010). Figure 16 shows the calculated fast neutron variations versus those same four measures. Parts A and B of each figure show <A> or fast neutron variations versus Fe and Mg concentrations. Parts C and D show <A> or fast neutrons versus Σ_{eff} (Prettyman et al. 2013) and C_p,

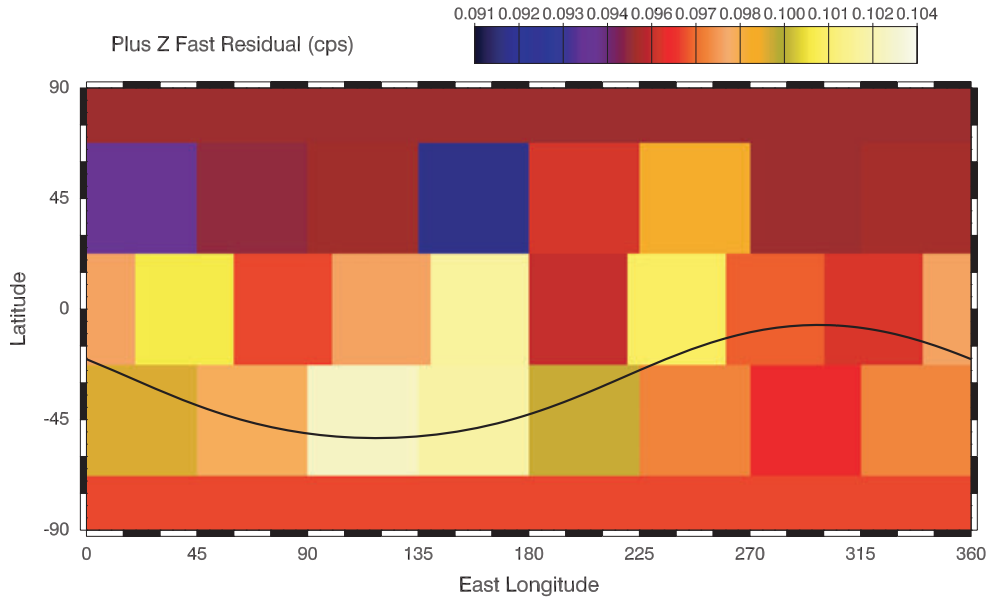

Fig. 14. Cylindrical projection map of +Z TTSP-restricted residual map after detrending the epithermal neutron correlation shown in Fig. 13.

which is a measure of bulk elemental composition derived from high-energy gamma ray measurements (Peplowski and Lawrence 2013; Peplowski et al. 2013).

Prettyman et al. (2011) discussed how <A> varies with various elements within HED meteorites and we both summarize and expand that discussion here, comparing meteorite compositional trends with compositional variability on Vesta's surface. Meteorite data shown in Figs. 15A and 16A show a general correlation between <A> and fast neutrons with Fe concentrations, but neither <A> nor fast neutrons are monotonically related to Fe concentrations. In both cases, the highest Fe concentrations seen in basaltic eucrites also reflect the largest <A> and fast neutron values. The orbital data confirms this relationship where the highest residual fast neutron counts are seen in nonpolar regions around longitudes 90ºE to 225ºE (Fig. 10) that also show some of the highest Fe concentrations (Yamashita et al. 2013). However, relatively low residual fast neutron count rates are seen in the north polar region, while Yamashita et al. (2013) report relatively high Fe concentrations in the north polar region. For meteorites that have more modest-to-low Fe concentrations, the plots of Figs. 15A and 16A suggest that <A> (or fast neutrons) might or might not have correspondingly low values. The orbital data support this idea, where a lobe of low Fe concentrations near 60ºE longitude is not matched by equally low fast neutrons. Yet, on the western portion of Vesta (approximately 270ºE to 315ºE), there are lobes of low Fe concentrations and fast neutrons that roughly correspond to each other. Finally, meteoritic Fe and <A> (or fast neutrons) show lower values for diogenite materials. The orbital data agree with the meteorite data and show lower Fe and fast neutron count rates in Rheasilvia basin, which is regarded as enriched in diogenite material (e.g., De Sanctis et al. 2012; Reddy et al. 2012; Prettyman et al. 2012; 2013; Peplowski et al. 2013; Yamashita et al. 2013).

In contrast to Fe, Mg concentrations have a tighter anticorrelation with <A> (Fig. 15B). There is a less tight anticorrelation of fast neutrons with Mg (Fig. 16), where meteorite groups with moderate Mg and fast neutron values (cumulate eucrite and howardite) do not show a strong Mg versus fast neutron trend. We note that, based on the Usui and McSween (2007) and Usui et al. (2010) database, and as also noted by Prettyman et al. (2011, 2012, 2013), other major elements such as Al and Ca show strong anticorrelations with Mg, with the possible exception of cumulate eucrites, which do not appear to show as strong a correlation for these elements. Thus, for most HED groups, when Mg is known, Al and Ca can also be determined. From these observations, the low fast neutron counts within the northern polar region suggest that this region is enriched in Mg concentrations relative to other portions of Vesta. However, the relatively high Fe concentrations in the north polar region (Yamashita et al. 2013) combined with fast neutron and HEGR results suggest that HED meteorites might not best explain Vesta's northern composition and/or there may be remaining systematic uncertainties within the various orbital data sets for this region (Prettyman et al. 2013).

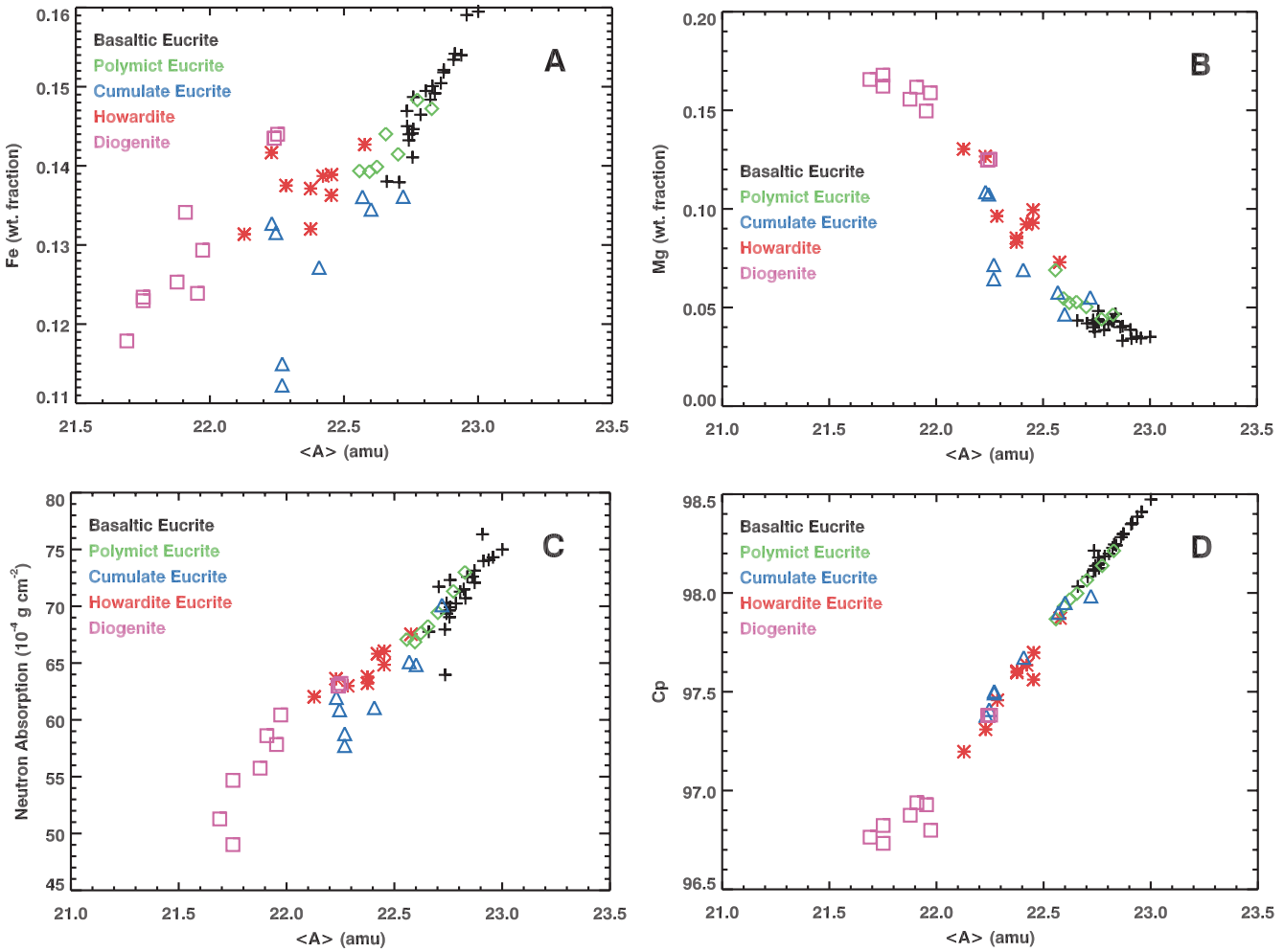

Fig. 15. <A> values versus element concentrations and GRaND measurables as determined for 57 meteorite compositions from Usui and McSween (2007) and Usui et al. (2010). Different colors and symbols represent different HED classes. A) Fe concentration versus <A>; B) Mg concentration versus <A>; C) Neutron absorption Σ_{eff} versus <A>; D) C_p versus <A>.

Variation of Residual Fast Neutrons with Neutron Absorption and High-Energy Gamma Rays

A comparison of <A> and calculated fast neutrons with variations in neutron absorption and HEGRs shows interesting features for both the meteorite and orbital data. Figures 15C and 15D show that the neutron absorption Σ_{eff} and the HEGR compositional parameter C_p correlate relatively well with <A>; C_p shows a tighter correlation with <A> than Σ_{eff} versus <A>. The direct, linear correlation between Σ_{eff} and <A> is not as strong for diogenites and cumulate eucrites as for the other meteorite groups. Basaltic eucrites show the best correlation of <A> with both Σ_{eff} and C_p. Correlations are less pronounced for Σ_{eff} and C_p versus fast neutrons. As with the <A> plots, fast neutrons show the tightest correlation with Σ_{eff} and C_p for basaltic eucrites. However, the other meteorite groups show little correlation between Σ_{eff} and fast neutrons. The correlations between fast neutrons and C_p are stronger, but, even here, there is little correlation between these values for howardite and cumulate eucrites. As a consequence, if the simulated fast neutron counts of HED meteorites accurately represent the measured fast neutrons, these values suggest that, for some classes of HED materials, Σ_{eff} and C_p are sensitive to different aspects of soil composition than fast neutrons.

A comparison of the residual fast neutron map (Fig. 10) with maps of Σ_{eff} (Prettyman et al. 2013) and C_p (Peplowski et al. 2013) tells a similar story. The equatorial region on Vesta that has been identified as rich in basaltic eucrites is also seen to have high values of Σ_{eff}, C_p, and fast neutrons. These observations are consistent with the presence of abundant basaltic eucrites. All three measurements show low or relatively low values in Rheasilvia basin, which is consistent with

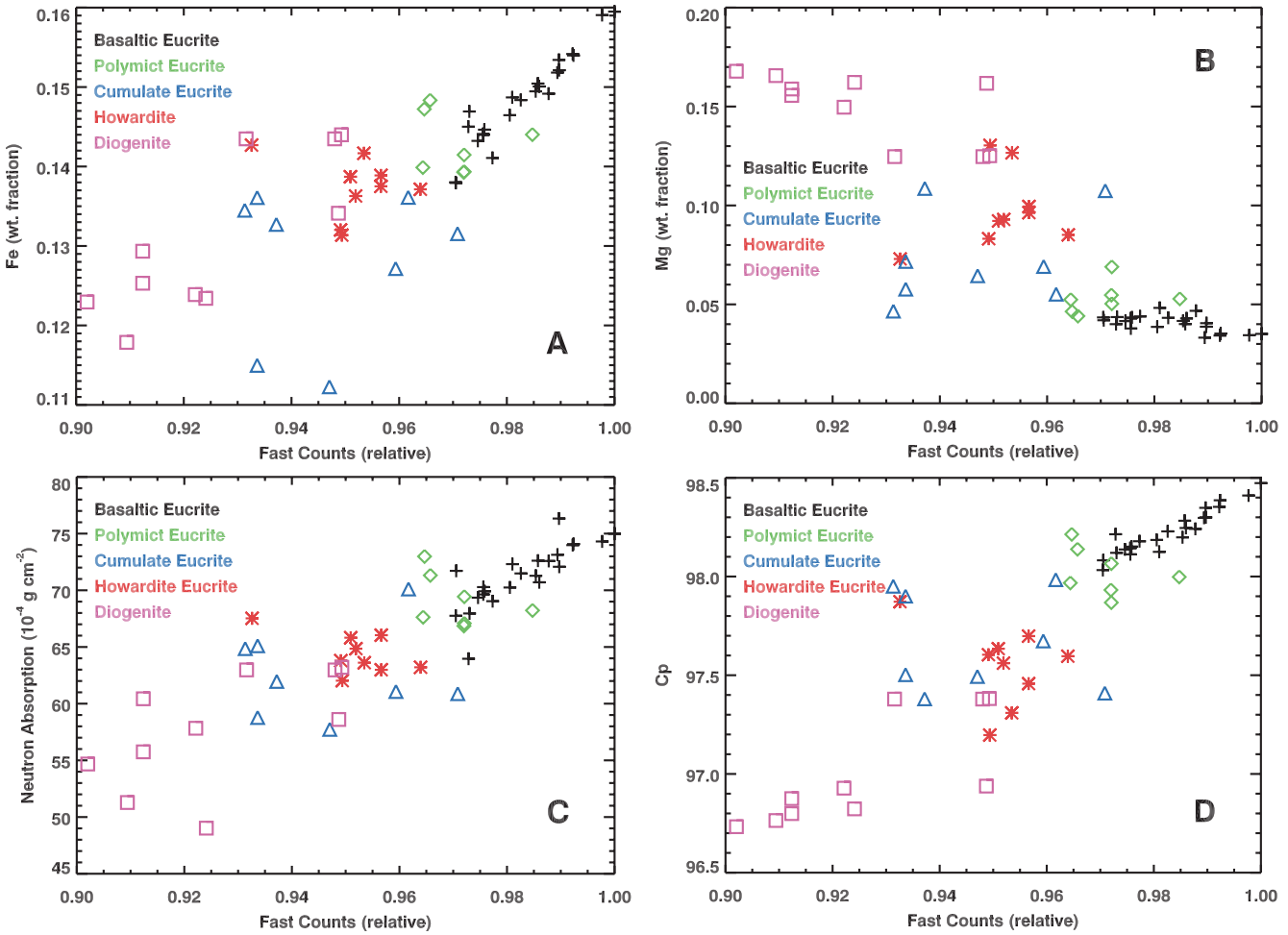

Fig. 16. Calculated fast neutron count rates versus element concentrations and GRaND measurables as determined for 57 compositions from Usui and McSween (2007) and Usui et al. (2010). Different colors and symbols represent different HED classes. A) Fe concentration versus fast neutrons; B) Mg concentration versus fast neutrons; C) Σ_{eff} versus fast neutrons; D) C_p versus fast neutrons.

the presence of diogenite-rich material. Despite these areas of agreement, there are multiple locations where the relative count rates from the three measurements do not match. Equatorial longitudes west of 90ºE have a relatively low Σ_{eff} values, but moderate values of C_p and fast neutrons. This is consistent with the presence of a nonbasaltic material where fast neutrons do not necessarily correlate with neutron absorption (or with Fe, as was pointed out earlier), such as a diogenite or cumulate eucrite lithology. The north polar region shows a different scenario where both fast neutrons and C_p show relatively low values, but neutron absorption has moderate values. Again, these measurements are indicative of a nonbasaltic material where fast neutrons and neutron absorption do not correlate, but this region has a different compositional character than the equatorial region west of 90ºE.

We finally note count rates in two other locations where we compare fast neutrons with C_p values. The first location is a region around 270ºE to 315ºE and near the equator. This region has an enhancement of C_p values without a corresponding fast neutron enhancement. The second location is between 45ºE and 135ºE and north of the equator. This region shows relatively low C_p values, but moderate fast neutron values. Given the observation that fast neutrons and C_p values show a strong correlation for almost all HED meteorite types for the whole-rock compositions tested, these two differences are notable. From Fig. 16B, one suggestion is that these locations could be associated with cumulate eucrite materials, for which the fast neutron-to-C_p correlation does not appear to hold. Both of these regions are near locations that have been identified as having orange colored ejecta from Oppia

crater (8ºS, 309ºE; Reddy et al. 2012; Le Corre et al. 2013) and Arruntia crater (39ºN, 72ºE; Le Corre et al. 2013). Several possible ideas have been suggested to explain the dominant composition of the orange material (Le Corre et al. 2013), including olivine enrichment, metal-rich material, and impact melts or shocked materials. GRaND fast neutron data might aid in discriminating among different hypotheses for the petrology of these regions. However, more work is needed to understand the compositional character of HEDs in relation to simulated and measured fast neutrons to realize the full potential of the fast neutron data set.

SUMMARY

We have presented a full analysis of GRaND fast neutron data from low-altitude mapping by the Dawn mission at Vesta. The epithermal neutron-detrended fast neutron data show clear compositional variations that are consistent in magnitude with expected variations in HED meteorites, thus providing further evidence of the compositional link between Vesta and HED meteorites (Russell et al. 2012). In particular, there is a relative fast neutron enhancement in the eastern equatorial region that is consistent with higher Fe concentrations as well as relative enhancements in high-energy gamma rays and neutron absorption parameters. This same general region also shows an enhancement in hydrogen and is consistent with having a basaltic eucrite composition. Fast neutrons show a relative decrease in the Rheasilvia basin and this general decrease is consistent with prior assessments that this region dominantly contains a diogenite-type composition. Fast neutrons also show a relative decrease in the northern latitudes of Vesta. Based on fast neutron-to-major element correlations, these northern regions may have enhanced Mg concentrations compared with other locations on Vesta. While there are similarities between the spatial distribution of fast neutrons and other GRaND measurements, there remain notable differences that may be indicative of real compositional variability at Vesta's surface. More work needs to be done to understand how systematic elemental variations, most importantly for cumulate eucrites, relate to measured fast neutrons. Finally, using TTSP-restricted fast neutron data, we find broad agreement with Prettyman et al. (2012) that Vesta's surface has variable hydrogen concentrations with a lower limit concentration estimate of 400 ppm H.

Acknowledgments—The authors thank two anonymous reviewers who provided helpful and constructive comments, which resulted in a much improved manuscript. The Dawn mission is led by the University of California, Los Angeles, and managed by the Jet Propulsion Laboratory, Pasadena, California under the auspices of the NASA Discovery Program Office. Support for this work was provided by the Dawn mission program and by NASA's Dawn at Vesta Participating Scientist program. Science experimental data records and housekeeping data acquired by GRaND during Vesta encounter and used in this study are available from NASA's Planetary Data System.

Editorial Handling—Dr. Harry Y. McSween Jr.

REFERENCES

Boynton W., Feldman W., Mitrofanov I., Evans L., Reedy R., Squyres S., Starr R., Trombka J., d'Uston C., and Arnold J. 2004. The Mars Odyssey gamma-ray spectrometer instrument suite. *Space Science Reviews* 110:37–83.

De Sanctis M. C., Ammannito E., Capria M. T., Tosi F., Capaccioni F., Zambon F., Carraro F., Fonte S., Frigeri A., Jaumann R., Magni G., Marchi S., McCord T. B., McFadden L. A., McSween H. Y., Mittlefehldt D. W., Nathues A., Palomba E., Pieters C. M., Raymond C. A., Russell C. T., Toplis M. J., and Turrini D. 2012. Spectroscopic characterization of mineralogy and its diversity across Vesta. *Science* 336:697–700.

Feldman W. C., Maurice S., Binder A. B., Barraclough B. L., Elphic R. C., and Lawrence D. J. 1998. Fluxes of fast and epithermal neutrons from Lunar Prospector: Evidence for water ice at the lunar poles. *Science* 281:1496–1500.

Feldman W. C., Boynton W., Tokar R., Prettyman T., Gasnault O., Squyres S., Elphic R., Lawrence D., Lawson S., and Maurice S. 2002. Global distribution of neutrons from Mars: Results from Mars Odyssey. *Science* 297:75–78.

Feldman W. C., Ahola K., Barraclough B. L., Belian R. D., Black R. K., Elphic R. C., Everett D. T., Fuller K. R., Kroesche J., Lawrence D. J., Lawson S. L., Longmire J. L., Maurice S., Miller M. C., Prettyman T. H., Storms S. A., and Thornton G. W. 2004. The gamma-ray, neutron, and alpha-particle spectrometers for the Lunar Prospector mission. *Journal of Geophysical Research: Planets* 109: E07S06, doi:10.1029/2003JE002207.

Feldman W. C., Mellon M. T., Gasnault O., Diez B., Elphic R. C., Hagerty J. J., Lawrence D. J., Maurice S., and Prettyman T. H. 2007. Vertical distribution of hydrogen at high northern latitudes on Mars: The Mars Odyssey Neutron Spectrometer. *Geophysical Research Letters* 34: L05201, doi:10.1029/2006GL028936.

Gasnault O., d'Uston C., Feldman W. C., and Maurice S. 2000. Lunar fast neutron leakage flux calculation and its elemental abundance dependence. *Journal of Geophysical Research* 105:4263–4271.

Gasnault O., Feldman W. C., Maurice S., Genetay I., d'Uston C., Prettyman T. H., and Moore K. R. 2001. Composition from fast neutrons: Application to the Moon. *Geophysical Research Letters* 28:3797–3800.

Goldsten J. O., Rhodes E. A., Boynton W. V., Feldman W. C., Lawrence D. J., Trombka J. I., Smith D. M., Evans L. G., White J., and Madden N. W. 2007. The MESSENGER gamma-ray and neutron spectrometer. *Space Science Reviews* 131:339–391.

Lawrence D. J., Feldman W., Elphic R., Hagerty J., Maurice S., McKinney G., and Prettyman T. 2006. Improved modeling of Lunar Prospector neutron spectrometer data: Implications for hydrogen deposits at the lunar poles. *Journal of Geophysical Research* 111:E08001, doi:10.1029/2005JE002637.

Lawrence D. J., Feldman W. C., Goldsten J. O., Maurice S., Peplowski P. N., Anderson B. J., Bazell D., McNutt R. L., Nittler L. R., Prettyman T. H., Rodgers D. J., Solomon S. C., and Weider S. Z. 2013. Evidence for water ice near Mercury's north pole from MESSENGER neutron spectrometer measurements. *Science* 339:292–296.

Le Corre L., Reddy V., Schmedemann N., Becker K. J., O'Brien D. P., Yamashita N., Peplowski P. N., Prettyman T. H., Li J., Cloutis E. A., Denevi B. W., Kneissl T., Palmer E., Gaskell R., Nathues A., Gaffey M. J., Mittlefehldt D. W., Garry W. B., Sierks H., Russell C. T., Raymond C., De Sanctis M. C., and Ammanito E. 2013. Olivine or impact melt: Nature of the orange material on Vesta from Dawn observations. *Icarus* 226:1568–1594, doi:10.1016/j.icarus.2013.08.013.

Maurice S., Feldman W. C., Lawrence D. J., Gasnault O., d'Uston C., and Lucey P. G. 2000. High-energy neutrons from the Moon. *Journal of Geophysical Research* 105:20365–20375.

Maurice S., Feldman W., Diez B., Gasnault O., Lawrence D., Pathare A., and Prettyman T. 2011. Mars Odyssey neutron data: 1. Data processing and models of water-equivalent-hydrogen distribution. *Journal of Geophysical Research* 116:E11008.

Pelowitz D. B. 2007. *MCNPX User's Manual, Version 2.5.0*. Report LA-UR-94-1817. Los Alamos, New Mexico: Los Alamos National Laboratory.

Peplowski P. N. and Lawrence D. J. 2013. New insights into the global composition of the lunar surface from high-energy gamma rays measured by Lunar Prospector. *Journal of Geophysical Research: Planets*, doi:10.1002/jgre.20063.

Peplowski P. N., Lawrence D. J., Prettyman T. H., Yamashita N., Bazell D., Feldman W. C., Le Corre L., McCoy T. J., Reddy V., Reedy R. C., Russell C. T., and Toplis M. J. 2013. Compositional variability on the surface 1 of 4 Vesta revealed through GRaND measurements of high-energy gamma rays. *Meteoritics & Planetary Science*, doi:10.1111/maps.12176.

Prettyman T. H., Feldman W. C., Mellon M. T., McKinney G. W., Boynton W. V., Karunatillake S., Lawrence D. J., Maurice S., Metzger A. E., Murphy J. R., Squyres S. W., Starr R. D., and Tokar R. L. 2004. Composition and structure of the Martian surface at high southern latitudes from neutron spectroscopy. *Journal of Geophysical Research* 109:E05001, doi:10.1029/2003JE002139.

Prettyman T. H., Feldman W., McSween H., Dingler R., Enemark D., Patrick D., Storms S., Hendricks J., Morgenthaler J., Pitman K., and Reedy R. 2011. Dawn's gamma ray and neutron detector. *Space Science Reviews* 163:371–459.

Prettyman T. H., Mittlefehldt D. W., Yamashita N., Lawrence D. J., Beck A. W., Feldman W. C., McCoy T. J., McSween H. Y., Toplis M. J., Titus T. N., Tricarico P., Reedy R. C., Hendricks J. S., Forni O., Le Corre L., Li J.-Y., Mizzon H., Reddy V., Raymond C. A., and Russell C. T. 2012. Elemental mapping by Dawn reveals exogenic H in Vesta's regolith. *Science* 338:242–246.

Prettyman T. H., Mittlefehldt D. W., Yamashita N., McSween H. Y., Hendricks J. S., Lawrence D. J., Peplowski P. N., Feldman W. C., Reedy R. C., Le Corre L., Reddy V., Titus T. N., Toplis M. J., Mizzon H., Beck A. W., McCoy T., Raymond C. A., and Russell C. T. 2013. Neutron absorption constraints on the composition of 4 Vesta. *Meteoritics & Planetary Science*, doi:10.1111/maps.12244.

Reddy V., Nathues A., Le Corre L., Sierks H., Li J.-Y., Gaskell R., McCoy T., Beck A. W., Schröder S. E., Pieters C. M., Becker K. J., Buratti B. J., Denevi B., Blewett D. T., Christensen U., Gaffey M. J., Gutierrez-Marques P., Hicks M., Keller H. U., Maue T., Mottola S., McFadden L. A., McSween H. Y., Mittlefehldt D., O'Brien D. P., Raymond C., and Russell C. 2012. Color and albedo heterogeneity of Vesta from Dawn. *Science* 336:700–704.

Russell C. and Raymond C. 2011. The Dawn Mission to Vesta and Ceres. *Space Science Reviews* 163:3–23.

Russell C. T., Raymond C. A., Coradini A., McSween H. Y., Zuber M. T., Nathues A., De Sanctis M. C., Jaumann R., Konopliv A. S., Preusker F., Asmar S. W., Park R. S., Gaskell R., Keller H. U., Mottola S., Roatsch T., Scully J. E. C., Smith D. E., Tricarico P., Toplis M. J., Christensen U. R., Feldman W. C., Lawrence D. J., McCoy T. J., Prettyman T. H., Reedy R. C., Sykes M. E., and Titus T. N. 2012. Dawn at Vesta: Testing the protoplanetary paradigm. *Science* 336:684–686.

Usui T. and McSween H. Y. 2007. Geochemistry of 4 Vesta based on HED meteorites: Prospective study for interpretation of gamma ray and neutron spectra for the Dawn mission. *Meteoritics & Planetary Science* 42:255–269.

Usui T., McSween H. Y., Jr., Mittlefehldt D. W., and Prettyman T. H. 2010. K-Th-Ti systematics and new three-component mixing model of HED meteorites: Prospective study for interpretation of gamma-ray and neutron spectra for the Dawn mission. *Meteoritics & Planetary Science* 45:1170–1190.

Yamashita N., Prettyman T. H., Mittlefehldt D. W., Toplis M. J., McCoy T. J., Beck A W., Reedy R. C., Feldman W. C., Lawrence D. J., Peplowski P. N., Forni O., Mizzon H., Raymond C. A., and Russell C. T. 2013. Distribution of iron on Vesta. *Meteoritics & Planetary Science*, doi:10.1111/maps.12139.

APPENDIX

AFTERPULSING ANALYSIS OF +Z AND −Y SENSORS

Here, we describe an analysis of afterpulsing that was carried out using Vesta LAMO data. Afterpulsing occurs when the PMT emits a low-amplitude pulse 1–2 μs after a primary pulse. This second pulse is caused by the ionization of residual gas within the PMT. Double-event data from the −Y sensor are shown in Figs. A1 and A2. For each figure, part A shows a count rate contour plot as a function of TTSP and first pulse amplitude; part B shows a TTSP histogram that is similar to Figs. 3B and 4B. Figure A1 shows −Y data

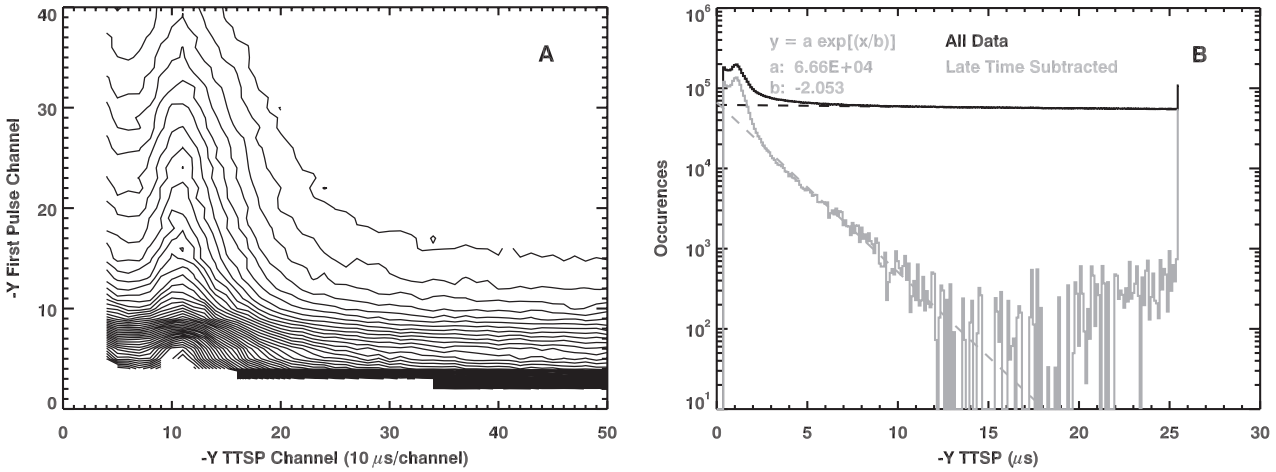

Fig. A1. a) Contour values of neutron count rates as a function of -Y TTSP channel and −Y first pulse amplitude for a second pulse threshold of 2 channels. b) −Y sensor TTSP values for a second pulse threshold of 2 channels. Solid black line shows the full data set, dashed black line shows an exponential function fitted to late times, solid gray line shows a late-time subtracted TTSP histogram, and dashed gray line shows an exponential function fitted to the late-time subtracted data. The fit parameters for the late-time subtracted data are shown.

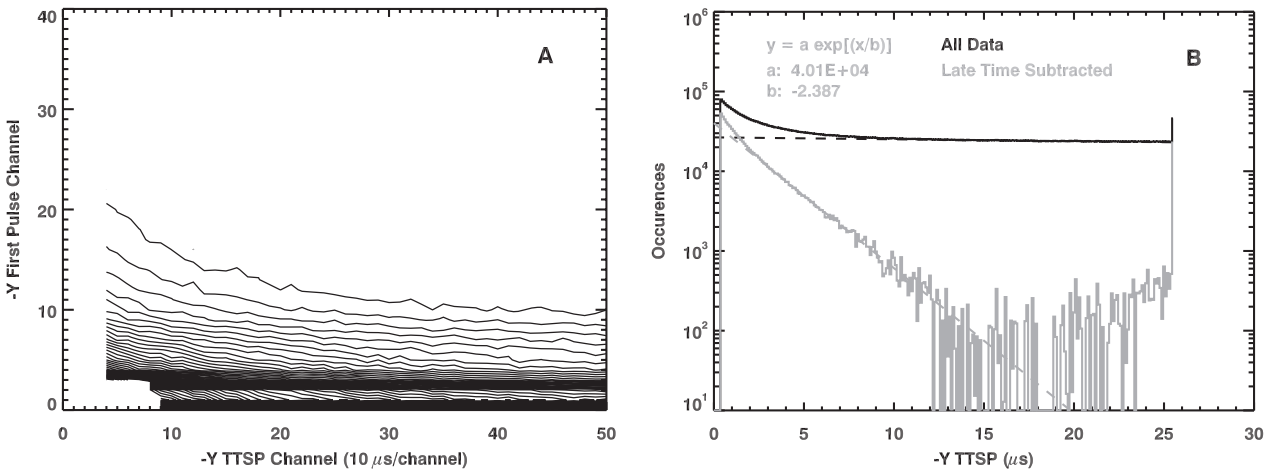

Fig. A2. Same plots as for Fig. A1, but for the −Y sensor with a second pulse threshold of 15 channels.

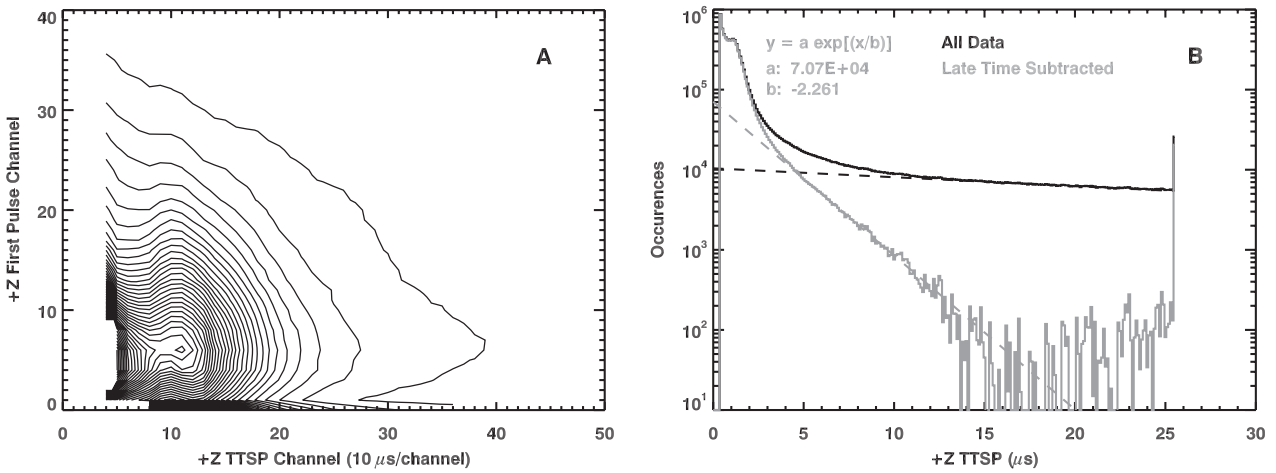

Fig. A3. Same plots as for Fig. A1, but for the +Z sensor with a second pulse threshold of 2 channels.

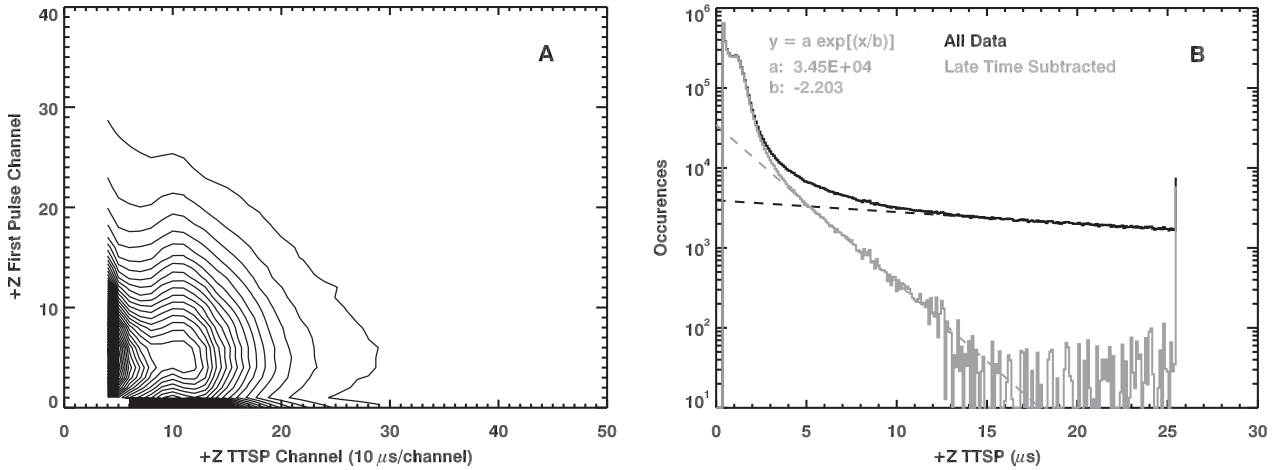

Fig. A4. Same plots as for Fig. A1, but for the +Z sensor with a second pulse threshold of 15 channels.

when a threshold of two channels has been applied to the second pulse. Both plots show a TTSP peak around 1 μs. Figure A1 shows that this peak is not dependent on the first pulse amplitude as it is located at a fixed TTSP value. Figure A2 shows the same type of values as Fig. A1, but when a threshold of 15 channels has been applied to the second pulse. The 1 μs TTSP peak has been removed, which is a clear indication that the peak in Fig. A1 is due to after-pulsing. Double-event data from the +Y sensor (not shown) has the same behavior as those for the −Y sensor.

Figures A3 and A4 show the same types of data for the +Z sensor as is shown in Figs. A1 and A2 using the same second pulse thresholds. For the second pulse channel 2 threshold data, the TTSP histogram (Fig. A3b) shows a 1 μs peak that looks similar to the −Y sensor data. However, the first pulse versus TTSP contour plot shows a qualitatively different distribution than is seen with the −Y sensor. Specifically, the count rate distribution is asymmetric and spread out in TTSP values, and concentrated at lower first pulse values. Further, when a second pulse threshold of 15 channels is applied (Fig. A4), the first pulse versus TTSP distribution is unchanged. Such behavior is not consistent with after-pulsing. Double-event data from the −Z phoswich sensor (not shown) illustrate the same behavior as shown here for the +Z phoswich sensor. When this information is combined with the second pulse histogram (Fig. 3B) that shows clear $^{10}B(n,\alpha)$ detections in the +Z sensor, we conclude that the 1 μs TTSP peak seen in the +Z sensor is not due to afterpulsing and is probably due to effects from a combination of the Li glass borated plastic phoswich arrangement and/or the electronics used to read out these sensors.